

Article

# Structural Characterization of Iron Meteorites through Neutron Tomography

Stefano Caporali <sup>1,2,†,\*</sup>, Francesco Grazzi <sup>3,†</sup>, Filomena Salvemini <sup>3,4</sup>, Ulf Garbe <sup>4</sup>, Steven Peetermans <sup>5,‡</sup> and Giovanni Pratesi <sup>6</sup>

<sup>1</sup> Consorzio Interuniversitario Nazionale per la Scienza e Tecnologia di Materiali (INSTM), Firenze 50123, Italy

<sup>2</sup> Dipartimento di Chimica, Università degli studi di Firenze, Sesto Fiorentino, FI 50019, Italy

<sup>3</sup> Consiglio Nazionale delle Ricerche, Istituto dei Sistemi Complessi, Sesto Fiorentino, FI 50019, Italy; francesco.grazzi@fi.isc.cnr.it (F.G.); filomens@ansto.gov.au (F.S.)

<sup>4</sup> Bragg Institute, Australian Nuclear Science and Technology Organisation (ANSTO), Lucas Height, NSW 2234, Australia; Ulf.Garbe@ansto.gov.au

<sup>5</sup> Paul Scherrer Institut, Swiss Spallation Neutron Source (SINQ) Neutron Source, Villigen 5232, Switzerland; Steven.Peetermans@psi.ch

<sup>6</sup> Museo di Storia Naturale, Università degli studi di Firenze, Firenze 50123, Italy; g.pratesi@unifi.it

\* Correspondence: stefano.caporali@unifi.it; Tel.: +39-055-457-3146

† These authors contributed equally to this work.

‡ Current address: AV Controlatom, Vilvoorde 1800, Belgium

Academic Editors: Jesus Martinez-Frias and Hasnaa Chennaoui

Received: 13 January 2016; Accepted: 16 February 2016; Published: 19 February 2016

**Abstract:** In this communication, we demonstrate the use of neutron tomography for the structural characterization of iron meteorites. These materials prevalently consist of metallic iron with variable nickel content. Their study and classification is traditionally based on chemical and structural analysis. The latter requires cutting, polishing and chemical etching of large slabs of the sample in order to determine the average width of the largest kamacite lamellae. Although this approach is useful to infer the genetical history of these meteorites, it is not applicable to small or precious samples. On the base of different attenuation coefficient of cold neutrons for nickel and iron, neutron tomography allows the reconstruction of the Ni-rich (taenite) and Ni-poor (kamacite) metallic phases. Therefore, the measure of the average width of the largest kamacite lamellae could be determined in a non-destructive way. Furthermore, the size, shape, and spatial correlation between kamacite and taenite crystals were obtained more efficiently and accurately than via metallographic investigation.

**Keywords:** iron meteorites; neutron imaging; neutron tomography; taenite; kamacite; non-destructive analysis

## 1. Introduction

Iron meteorites are assumed to be the splinter portions of ancient asteroid's core that, after extensive melting, separation of the metal from the silicate and more or less rapid crystallization, went shattered by hypervelocity impacts. The overwhelming bulk composition of these meteorites consists of Fe–Ni alloys; *i.e.*, kamacite ( $\alpha$ -(Fe,Ni), BCC structure) and taenite ( $\gamma$ -(Ni,Fe), FCC structure). Minor minerals (sulphides, phosphides) may occur as accessory phases.

Traditionally, iron meteorites are classified based on their structures; *i.e.*, the examination of the shape and size of the kamacite lamellae formed as consequence of exsolution from the taenite phase. The kamacite bandwidth is primarily dictated by the bulk chemical composition, *i.e.*, nickel content, and the cooling rate; the higher the nickel content the faster the cooling rate is, the smaller the kamacite bandwidths are. A scheme of the structural classification is represented in Table 1.

**Table 1.** Structural classification of iron meteorites (data from [1]).

Structural Class	Symbol	Kamacite Bandwidth (mm)
Hexahedrites	H	>50
Coarsest octahedrites	Ogg	3.3–50
Coarse octahedrites	Og	1.3–3.3
Medium octahedrites	Om	0.5–1.3
Fine octahedrites	Of	0.2–0.5
Finest octahedrites	Off	<0.2
Plessitic octahedrites	Opl	<0.2 spindles
Ataxites	D	<0.03

Even though, nowadays, the chemical classification based on Ni, Ge, Ga and Ir content is preferred with respect to structural classification [2], the two approaches support and agree with each other.

Other than for classification purposes, the study of the meteorite micro- and macro-structure can provide valuable information regarding the phenomena that happened after meteorite crystallization. For instance, plastic deformation and stresses or annealing processes (reheating) caused by impact shocks or movement of the overburden, affect the meteorite microstructure. It is well known that the same pristine material can present different features regarding the secondary stages of metamorphism suffered after crystallization.

Traditionally, structural data are obtained by means of metallographic investigations requiring cutting of large parts, if not all, of the sample. That is obviously not acceptable for unique or very rare samples. Furthermore, metallographic investigation is performed on randomly cut surfaces returning 2D images of a 3D distribution of metallic phases. Even if structural data are extracted by averaging the bandwidths obtained from mutually perpendicular sections and correction factors for single randomly oriented sections have been published [3,4], these methodologies invariably represent approximations of the real 3D crystal distribution.

Computed tomography (CT) is a method to acquire volumetric maps of the beam attenuation coefficient distribution of an object. The method has been principally developed for X-ray imaging for probing a sample interior, but it applies to neutrons as well. It uses radiographic projection images from many views to reconstruct the distribution of materials in the sample. Mostly, the projections are acquired with equiangular steps over either 180° or 360° to cover the whole sample. In the last decade, X-ray computed tomography (X-ray CT) has been successfully applied to the study of planetary materials, such as chondrites [5–12], stardust [13,14], and tektites [15,16].

Use of neutron computed tomography (NCT) is somewhere less common since the production of a parallel neutron beam of sufficient intensity and suitable energy range is technologically much more complex than an X-ray beam. Beamlines suitable for neutron tomography are few and began to appear at research facilities only in the late 1990s; thus, optimal imaging protocols are still under development. Contrast in NCTs is generated by local differences in the neutron cross section reflecting the elemental (and in some cases the isotopic) composition of the sample. Therefore, NCT investigations are preferentially performed for those objects where neutrons present higher contrast or provide a better sample penetration than conventional X-ray CT. Analogously to X-ray CT, NCT generate 3D datasets in which the specimen is represented by an array of volume elements or voxels, each of which is assigned a grayscale (or false color scale) that correlates with the neutron attenuation (or neutron transmissivity). To obtain the 3D feature of the object, the measurement of neutron transmissivity along different linear paths through the specimen are combined via a mathematical inversion process called reconstruction.

In principle X-ray CT and NCT, can be considered two complementary techniques; NCT is superior to X-Ray CT to study the interior of dense materials, such as large metallic items [17–20], characterized by large and quite similar X-ray absorption coefficients, impairing the determination of internal features. In spite of their utility to cope with problems that relate to Earth science, NCT

studies of geologic materials are few [21–23] and, to the best of our knowledge, this technique has not been applied yet to planetary materials apart from a grain determination and phase distribution measurement performed by the same experimental team as the Mont Dieu meteorite [24].

In this paper, we assess the suitability and usefulness of neutron computed tomography (NCT) to characterize the structural features of five different iron meteorites. The different attenuation capability (sum of neutron absorption and neutron scattering) of iron and nickel (see Table 2) allows to discern within the taenite (Ni-rich) and kamacite (Ni-poor) crystals. This capability was successfully used to reconstruct the 3D distribution, size, and shape of the kamacite lamellae. The structural data obtained by means of NCT, in non-destructive way, fully agree with literature data obtained via metallographic investigation.

**Table 2.** Neutron cross sections averaged for the natural isotopes composition for Ni and Fe [25].

Element	Scattering: Total Bound Cross Section (barn *)	Absorption: Cross Section for 2200 m/s Neutrons (barn *)
Ni	18.5	4.49
Fe	11.62	2.56

\*: 1 barn =  $1.10^{-24}$  cm<sup>2</sup>

## 2. Materials and Methods

### 2.1. Materials

All the meteorite samples were provided by the Museo di Storia Naturale dell'Università degli Studi di Firenze (Florence, Italy). In particular, the following samples have been studied: Seymchan, Sikhote-Alin, Agoudal, Campo del Cielo, and Muonionalusta. Table 3 summarizes the data of the investigated samples that were analyzed, as received without any pretreatment or preparation.

**Table 3.** Summary of the chemical and structural characteristics of the analyzed meteorites.

Catalogue Number	Meteorite Name	Chemical Group	Structural Group
MSN-RI3218	Seymchan	Pallasite	Coarse octahedrite (Og)
MSN-RI3219	Sikhote-Alin	IIAB	Coarsest octahedrite (Ogg)
MSN-RI3220	Agoudal	IIAB	Coarse octahedrite (Og)
MSN-RI3221	Campo del Cielo	IAB	Hexahedrite (H)
MSN-RI3222	Muonionalusta	IVA	Fine octahedrite (Of)

### 2.2. Methods

Two different experimental set-ups were tested; the Imaging with Cold Neutrons (ICON) beamline [26] at Swiss Spallation Neutron Source (SINQ) at the Paul Scherrer Institut (Switzerland) and the DINGO beamline [27,28] at the Australian Nuclear Science and Technology Organisation (ANSTO, Lucas Heights, Australia). Details regarding the beamlines' properties and set-ups are reported below. It is important to mention here that the two beamlines use neutrons with different energies; cold neutrons were used at ICON (average wavelength of 3.1 Å), while thermal neutrons were employed at DINGO (wavelength distribution centered on 1.8 Å). Even if both the facilities allow kamacite and taenite discrimination, cold neutrons (ICON beam line) provide higher differences in signal attenuation, as the absorption cross-section scales linearly with the wavelength, resulting in a better image contrast.

In both cases, the projection images are acquired using a combination of a scintillator to convert the neutrons to visible light and a CCD camera and the transform of the projection data into a three dimensional image was performed using the Octopus code [29] for tomographic reconstruction.

Voxel resolution was  $13 \times 13 \times 13 \mu\text{m}^3$  in ICON and  $25 \times 25 \times 25 \mu\text{m}^3$  in DINGO. The obtained slices have been recomposed using the VGstudio code [30]. During the reconstruction process, virtual slices perpendicular to the rotation axis are produced. When these slices are stacked in a sequence, they form a three-dimensional volume image of the sample. The reconstructed volume data were visualized using three-dimensional rendering graphics software. Using such tools, regions can be segmented based on their attenuation coefficients and geometries, revealing details inside the sample in three dimensions. The peculiar characteristics of the two instrumental set-ups are described as follows.

Investigations using neutrons generally induce some sample activation due to the generation of radioactive nuclides from stable isotopes through neutron capture. However, neutron activation analysis measurements were carried out on the samples after a few first radiographies to make sure no radioactive isotopes with a long half-life would be formed during long neutron exposure times in NCT and the sample could be returned safely to the museum.

### 2.2.1. ICON Experimental Set-Up

ICON beamline at the the Paul Scherrer Institut is a dedicated beamline for imaging, with cold neutrons situated at beam port 52 around the SINQ spallation neutron source. The neutrons are generated by spallation of a lead target impinged by a quasi-continuous proton beam of 590 MeV and 1.5 mA. They are thermalized in a surrounding  $\text{D}_2\text{O}$  tank at room temperature, with a smaller tank of liquid  $\text{D}_2$  at 25 K. The transmitted neutron beam is converted into visible light using a scintillator, which is then guided via a mirror to a light-sensitive optical camera. For the experiments described above, a 100- $\mu\text{m}$  thick  $^6\text{Li}$  ZnS scintillator was used in combination with a DW434 CCD camera (Andor, Belfast, Northern Ireland) with  $1024 \times 1024$  pixels<sup>2</sup>. During the tomographic scan, projections were acquired with an equiangular step of  $0.576^\circ$  over  $360^\circ$  and an exposure time of 100 s each.

Further details about the beamlines can be found in the literature [26].

### 2.2.2. DINGO Experimental Set-Up

DINGO is located on the thermal beam HB-2, tangentially facing the 20 MW Open Pool Australian Lightwater (OPAL) reactor. A special feature of the instrument is the in-pile collimator place in front of the main shutter. The collimator offers two configurations, one for high speed and the other for high spatial resolution characterized by an L/D (Length to Diameter ratios) of 250 and 1000, respectively. A selector wheel allows setting one of the two and adjusting the beams size.

The high spatial resolution configuration was used for the neutron tomography analysis. The Andor IKON-L CCD camera (Andor, Belfast, Northern Ireland) was coupled with a 50- $\mu\text{m}$  thick ZnS/ $^6\text{LiF}$  scintillation screen and a Makro Planar 100 mm lens (Carl Zeiss, Jena, Germany) to obtain a pixel size of 25  $\mu\text{m}$ . During the tomographic scan, projections were acquired with an equiangular step of  $0.576^\circ$  over  $360^\circ$  and an exposure time of 110 s each.

Further details about the beamlines can be found in the literature [27,28].

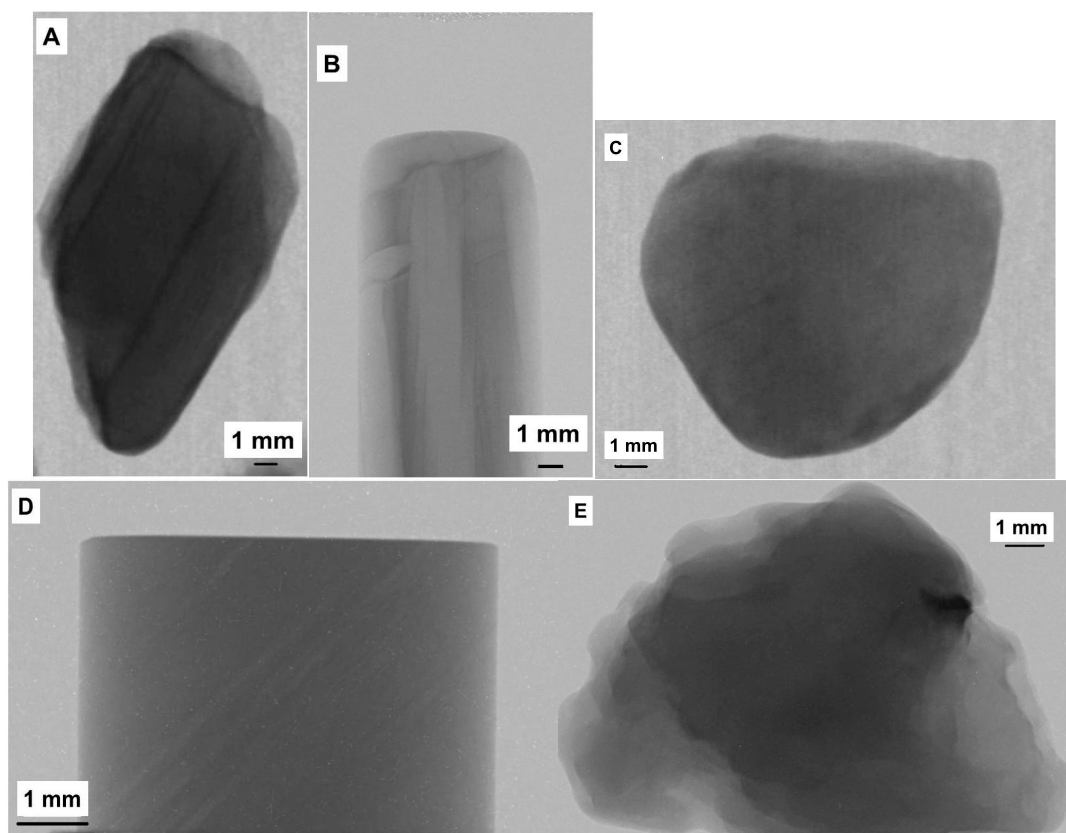
## 3. Results and Discussion

Figure 1 shows neutron transmission images of the meteorite samples investigated. Pixels of the material, characterized by large neutron attenuation are light, while the phases characterized by lower neutron attenuation (kamacite) are dark.

Tomographic dataset allow the 3D reconstruction of the samples. Videos of the rendered meteorites are presented in the Supplementary Materials (Videos S1 to S5).

In accordance with literature data, Agoudal, Sikote-Alin, and Campo del Cielo, present uniform internal structures. These meteorites are classified as coarsest or coarse octahedrites (see Table 1), which means that the kamacite crystals are larger than the investigated specimen (see Videos S1 to S3 in the Supplementary Materials). On the other hand, Seymchan is actually classified as pallasite (stony iron meteorite) with a coarse octahedrite metal phase [31,32]. The volume rendered image of the kamacite phase as determined by NCT data clearly shows two types of crystals. The larger presents an averaged

bandwidth of 2.8 mm, in agreement with the literature data. However, tiny (averaged bandwidth of 0.12–0.18 mm) exsolution lamellae are also detectable in the sample in the study (Figure 2A,B). Video of the reconstructed axial section is available in the Supplementary Materials (Video S4).



**Figure 1.** Neutron transmission radiographies of the meteorite samples investigated: (A) Agoudal; (B) Seymchan; (C) Sikhote-Alin; (D) Muonionalusta and (E) Campo del Cielo.

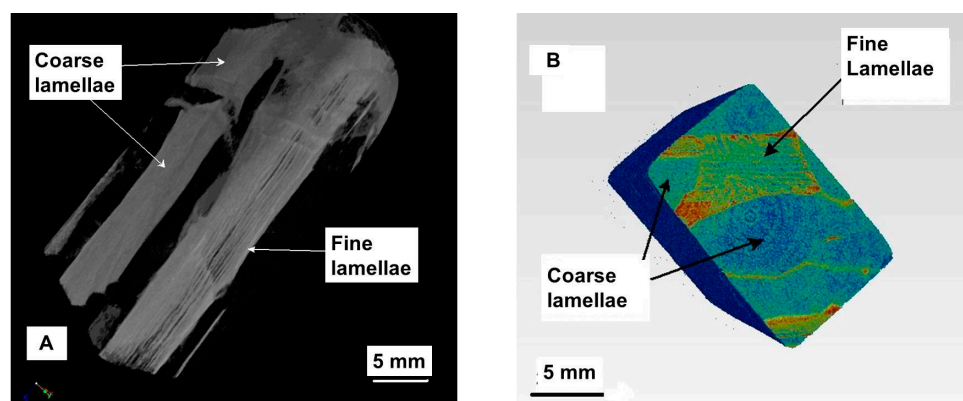


**Figure 2.** Volume rendered NCT image (A) of the Seymchan sample and (B) false color reconstructed axial section.

Even more interesting results were obtained by the rendering of the Muonionalusta dataset. The meteorite is characterized by a fine octahedral arrangement of kamacite in the parent taenite crystal. The isosurface 3D plot of the kamacite lamellae displayed in Figure 3 shows the octahedral arrangement. Video of the reconstructed axial section is available in the Supplementary Materials (Video S5).

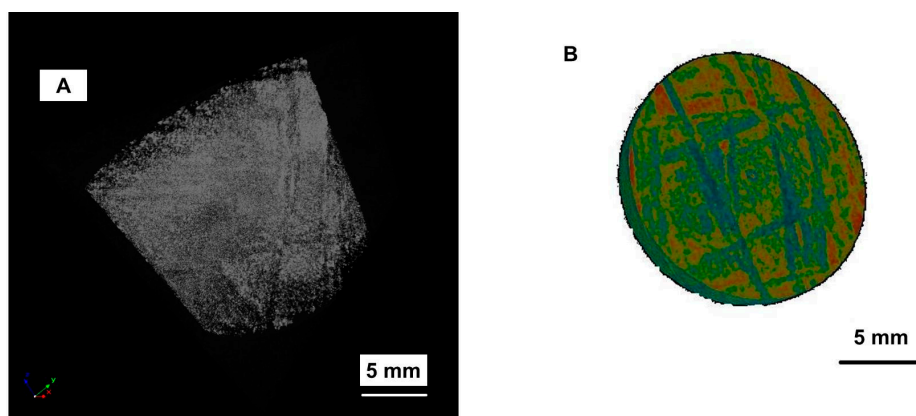


**Figure 3.** Volume rendered NCT image (A) of the Muonionalusta sample and (B) false color reconstructed axial section.

From the rendered 3D image, it is possible to determine the average bandwidth of kamacite lamellae that resulted in 0.23–0.28 mm. The size and shape of these lamellae, as well as their octahedral distribution, confirmed the structural classification of this meteorite as fine octahedrite.

These data assess the capability of NCT to determine the internal structure of metallic meteorites, allowing the 3D reconstruction of kamacite lamellae. For the instrumental set-ups, the applied neutron attenuation coefficients of iron and nickel results are different enough, allowing an unambiguous discrimination between Ni-rich (taenite) and Ni-poor (kamacite) phases.

#### 4. Conclusions

The use of neutron computer tomography (NCT) allowed the detailed characterization of the interior of iron meteorites, clearly discerning between Ni-rich (taenite) and Ni-poor (Kamacite) metallic phases. The evaluation of the size and shape of the kamacite lamellae allows the structural classification of the meteorite without any damage to the sample. The data obtained by means of NCT agree well with classical metallographic investigation, demonstrating the capability of this technique to provide detailed structural information of this class of planetary materials. The capacity of NCT to cope with spatial (3D) relationships between taenite and kamacite grains would be potentially very profitable. This, firstly, allows the non-destructive structural classification of iron meteorites, and, secondly, but perhaps as important, to provide information regarding the secondary stages of metamorphism, such as impacts and reheating, the meteorites suffered over the eons of time after its formation.

**Supplementary Materials:** The following are available online at [www.mdpi.com/2075-163X/6/1/14/s1](http://www.mdpi.com/2075-163X/6/1/14/s1), Video S1: False colors reconstructed NCT section of the Agoudal meteorite, Video S2: False colors reconstructed NCT section of the Sikote-Alin meteorite, Video S3: False colors reconstructed NCT section of the Campo del Cielo meteorite, Video S4: False colors reconstructed NCT section of the Seymchan meteorite, Video S5: False colors reconstructed NCT section of the Muonionalusta meteorite.

**Acknowledgments:** We would like to thank SINQ and OPAL staff for providing high quality neutron beams and support during the experiments.

**Author Contributions:** S.C. and F.G. conceived and designed the experiments and analyzed the data; G.P. selected the samples based on their morphologic, chemical, and structural properties. S.P. performed the experiments of the ICON beamline with F.S. and F.G., while F.S. performed the experiments and analyzed the data of the DINGO beamline. All the authors contributed to the writing of the paper.

**Conflicts of Interest:** The authors declare no conflicts of interest.

## Abbreviations

The following abbreviations are used in this manuscript:

X-Ray CT	X-Ray Computed Tomography
NCT	Neutron Computed Tomography
BCC	Body centered cubic
FCC	Face centered cubic

## References

1. Grady, M.M.; Pratesi, G.; Cecchi, V.M. *Atlas of Meteorites*, 1st ed.; Cambridge University Press: Cambridge, UK, 2014; pp. 322–329.
2. Wasson, J.T. *Meteorites: Classification and Properties*, 1st ed.; Springer-Verlag: Berlin, Germany, 1974; p. 316.
3. Frost, M.J. Kamacite plate width estimation in octahedrites. *Mineral. Magazine* **1965**, *35*, 640–642. [[CrossRef](#)]
4. Buchwald, V.F.B. *Handbook of Iron Meteorites*; University of California Press: Berkeley, CA, USA, 1975.
5. Hezel, D.C.; Friedrich, J.M.; Uesugi, M. Looking inside: 3D structures of meteorites. *Geochim. Cosmochim. Acta* **2013**, *116*, 1–4. [[CrossRef](#)]
6. Friedrich, J.M. Quantitative methods for three-dimensional comparison and petrographic description of chondrites. *Comput. Geosci.* **2008**, *34*, 1926–1935. [[CrossRef](#)]
7. Ebel, D.S.; Rivers, M.L. Meteorite 3-D synchrotron microtomography: Methods and applications. *Meteorit. Planet. Sci.* **2007**, *42*, 1627–1646. [[CrossRef](#)]
8. Hezel, D.C.; Elangovan, P.; Viehmann, S.; Howard, L.; Abel, R.L.; Armstrong, R. Visualisation and quantification of CV chondrite petrography using micro-tomography. *Geochim. Cosmochim. Acta* **2012**, *116*, 33–40. [[CrossRef](#)]
9. Uesugi, M.; Uesugi, K.; Takeuchi, A.; Suzuki, Y.; Hoshino, M.; Tsuchiyama, A. Three-dimensional observation of carbonaceous chondrites by synchrotron radiation X-ray CT—Quantitative analysis and developments for the future sample return missions. *Geochim. Cosmochim. Acta* **2013**, *116*, 17–32. [[CrossRef](#)]
10. Ebel, D.S.; Weisberg, M.K.; Hertz, J.; Campbell, A.J. Shape, metal abundance, chemistry and origin of chondrules in the Renazzo (CR) chondrite. *Meteorit. Planet. Sci.* **2008**, *43*, 1725–1740. [[CrossRef](#)]
11. Friedrich, J.M.; Macke, R.J.; Wignarajah, D.P.; Rivers, M.L.; Britt, D.T.; Ebel, D.S. Pore size distribution in an uncompactated equilibrated ordinary chondrite. *Planet. Space Sci.* **2008**, *56*, 895–900. [[CrossRef](#)]
12. Friedrich, J.M.; Rivers, M.L. Three-dimensional imaging of ordinary chondrite microporosity at 2.6  $\mu\text{m}$  resolution. *Geochim. Cosmochim. Acta* **2013**, *116*, 63–70. [[CrossRef](#)]
13. Tsuchiyama, A.; Nakamura, T.; Okazaki, T.; Uesugi, K.; Nakano, T.; Sakamoto, K.; Akaki, T.; Iida, Y.; Kadono, T.; Jogo, K.; *et al.* Three-dimensional structures and elemental distributions of Stardust impact tracks using synchrotron microtomography and X-ray fluorescence analysis. *Meteorit. Planet. Sci.* **2009**, *44*, 1203–1224. [[CrossRef](#)]
14. Ebel, D.S.; Greenberg, M.; Rivers, M.L.; Newville, M. Three-dimensional textural and compositional analysis of particle tracks and fragmentation history in aerogel. *Meteorit. Planet. Sci.* **2009**, *44*, 1445–1463. [[CrossRef](#)]
15. Rantzsch, U.; Franz, A.; Kloess, G. Moldavite porosity: A 3-D X-ray micro-tomography study. *Eur. J. Mineral.* **2013**, *25*, 705–710. [[CrossRef](#)]
16. Pratesi, G.; Caporali, S.; Loglio, F.; Giuli, G.; Dziková, L.; Skála, R. Quantitative Study of Porosity and Pore Features in Moldavites by Means of X-ray Micro-CT. *Materials* **2014**, *7*, 3319–3336. [[CrossRef](#)]
17. Lehmann, E.; Deschler-Erb, E.; Ford, A. Neutron tomography as a valuable tool for the non-destructive analysis of historical bronze sculptures. *Archaeometry* **2010**, *52*, 272–285. [[CrossRef](#)]
18. Barzagli, E.; Grazzi, F.; Salvemini, F.; Civita, F.; Scherillo, A.; Sato, H.; Shinohara, T.; Kamiyama, T.; Kiyonagi, Y.; Tremsin, A.; *et al.* Determination of the metallurgical properties of four ferrous Japanese arrow tips through Time of Flight Neutron Diffraction and Wavelength Resolved Neutron Transmission analysis: Identification of single crystal particles in historical metallurgy. *Eur. Phys. J. Plus* **2014**, *7*, 129–158.
19. Fedrigo, A.; Grazzi, F.; Williams, A.; Scherillo, A.; Civita, F.; Zoppi, M. Neutron diffraction characterization of Japanese armour components. *J. Anal. Atom. Spectrom.* **2013**, *286*, 908–915. [[CrossRef](#)]

20. Salvemini, F.; Grazzi, F.; Peetermans, S.; Civita, F.; Franci, R.; Hartmann, S.; Lehmann, E.; Zoppi, M. Quantitative characterization of Japanese ancient swords through energy-resolved neutron imaging. *J. Anal. Atom. Spectrom.* **2012**, *27*, 1494. [[CrossRef](#)]
21. Vontobel, P.; Lehmann, E.; Carlson, W.D. Comparison of X-ray and Neutron Tomography Investigations of Geological Materials. *IEEE Trans. Nucl. Sci.* **2005**, *52*, 338–341. [[CrossRef](#)]
22. Cnudde, V.; Dierick, M.; Vlassenbroeck, J.; Masschaele, B.; Lehmann, E.; Jacobs, P.; van Hoorebeke, L. High-speed neutron radiography for monitoring the water absorption by capillarity in porous materials. *Nucl. Instrum. Meth. B* **2008**, *266*, 155–163. [[CrossRef](#)]
23. Dawson, M.; Francis, J.; Carpenter, R. New views of plant fossils from Antarctica: A comparison of X-ray and neutron imaging techniques. *J. Paleontol.* **2014**, *88*, 702–707. [[CrossRef](#)]
24. Peetermans, S.; Grazzi, F.; Salvemini, F.; Lehmann, E.H.; Caporali, S.; Pratesi, G. Energy-selective neutron imaging for morphological and phase analysis of iron-nickel meteorites. *Analyst* **2013**, *138*, 5303–5308. [[CrossRef](#)] [[PubMed](#)]
25. Neutron Scattering Lengths and Cross Sections. Available online: <https://www.ncnr.nist.gov/resources/n-lengths/> (accessed on 28 December 2015).
26. Kaestner, A.P.; Hartmann, S.; Kühne, G.; Frei, G.; Grünzweig, C.; Josic, L.; Schmid, F.; Lehmann, E.H. The ICON beamline—A facility for cold neutron imaging at SINQ. *Nucl. Instr. Meth. A* **2011**, *659*, 387–393. [[CrossRef](#)]
27. Garbe, U.; Randall, T.; Hughes, C. The new neutron radiography/tomography/imaging station DINGO at OPAL. *Nucl. Instr. Meth. A* **2011**, *651*, 42–46. [[CrossRef](#)]
28. Garbe, U.; Randall, T.; Hughes, C.; Davidson, G.; Pangelis, S.; Kennedy, S.J. A new Neutron Radiography/Tomography/Imaging Station DINGO at OPAL. *Phys. Procedia* **2015**, *69*, 27–32. [[CrossRef](#)]
29. Dierick, M.; Masschaele, B.; van Hoorebeke, L. Octopus, a fast and user-friendly tomographic reconstruction package developed in LabView (R). *Meas. Sci. Technol.* **2004**, *15*, 1366–1370. [[CrossRef](#)]
30. VGstudio. Available online: <http://www.volumegraphics.com/en/products/vgstudio/basic-functionality/> (accessed on 28 December 2015).
31. Van Niekerk, D.; Greenwood, R.C.; Franchi, I.A.; Scott, E.R.D.; Keil, K. Seymchan: A main group pallasite—Not an iron meteorite. *Meteorit. Planet. Sci. Suppl.* **2004**, *42*, 5196.
32. Scott, E.R.D.; Wasson, J.T. Chemical classification of iron meteorites—VIII. Groups IC, IIE, IIIF and 97 other irons. *Geochim. Cosmochim. Acta* **1976**, *40*, 103–115. [[CrossRef](#)]



© 2016 by the authors; licensee MDPI, Basel, Switzerland. This article is an open access article distributed under the terms and conditions of the Creative Commons by Attribution (CC-BY) license (<http://creativecommons.org/licenses/by/4.0/>).